Counting Active Sites for Nanocatalysis

Forrest H. Kaatz*[1] , Adhemar Bultheel[2] , and Dmitry Yu. Murzin[3]

[1] *Institutional Research, NMSU-Alamogordo, 2400 N. Scenic Drive, Alamogordo, NM 88310, USA.*
[2] *Department of Computer Science, KU Leuven, Celestijnenlaan 200A, 3001 Heverlee, Belgium.*
[3] *Industrial Chemistry and Reaction Engineering, Abo Akademi University, Henriksgatan 2, Turku, 20500 Finland.*
*Retired; Corresponding author: email: fhkaatz@gmail.com

Abstract

The topic of active sites on catalysts is of current interest, i.e. identifying and counting them, since this knowledge is relevant to improving chemical behavior. Previous work recognizes that catalytic activity is related to active sites via generalized coordination numbers (GCNs). The method we present uses magical formulas, which applies to general nanocatalysis, since it is related to mathematical properties of fcc nanostructures, and is not element specific. This method is demonstrated for platinum nanostructures, of interest for the oxidation reduction reaction (ORR). We model four polyhedral clusters, nanocages, and trilayer strained heteroepitaxial clusters. These geometric descriptors quantify the variables of morphology, size, and number of wall layers for these shapes. We use magical formulas for the GCNs to count active sites thus modeling mass activity for platinum clusters and nanocages with (111) facets having tetrahedral, icosahedral, and octahedral morphology, and (100) cubic symmetry. This model predicts that 20 nm octahedral cages with 3 wall layers will have a mass activity $\sim$ 3 A/mg$_{\mathrm{Pt}}$. This is a factor of 2 improvement over octahedral cages of 20 nm size with 6 wall layers. We provide a model of monolayer platinum shells with a strained epitaxial interlayer in ternary clusters, including Pd@Ir@Pt, Pd@Rh@Pt, Pd@Cu@Pt and Ir@Pd@Pt. The maximum predicted mass activity is $\sim$ 1.8 A/mg$_{\mathrm{Pt}}$ for tetrahedral sub-10 nm core-shell clusters with a copper interlayer. The generality of the approach is illustrated by a suggested study of the nitrogen reduction reaction (NRR), with fcc ruthenium as the catalyst for similar nanoclusters and cages.

Keywords: generalized coordination; mass activity; nanocages; platinum; ruthenium; magic formulas; core-shell ternary clusters

Introduction

There is currently motivation for identifying active sites allowing to account for the diversity of size and shapes in model and industrial nanocatalysts. Utilization of the linear free energy relationship gives a possibility to link the energy barrier with the reaction energy, thus kinetics with thermodynamics. In turn the reaction energies are described with a scaling relation based in the generalized coordination numbers (GCNs) [1], with ΔE being proportional to GCN. The established concept of GCNs originally applied to platinum nanoparticles [1], can be expanded to any nanocluster or nanocage [2]. In essence, GCN takes into account not only the first-coordination shell of the surface metal atoms, but also its second-coordination shell.

The approach of this work is related to mathematical properties of face centered cubic (fcc) nanostructures and is built upon the previous work of the authors where the magical formulae were derived for clusters and cages [3, 4]. This work leads to the derivation herein where we apply the method to GCNs, since magical formulas are just a counting relationship between structure and geometry of atom locations. The relationship to chemical activity comes from the correlations between GCNs and activity for platinum [5, 6], thus has application to the oxidation reduction reaction (ORR). Likewise, there exist correlations between GCNs and

nitrogen dissociation on ruthenium for the nitrogen reduction reaction (NRR) [7]. Given the hypothesis that a certain active site is relevant for catalytic activity, we provide techniques for counting such sites, allowing the calculations of activity for fcc nanostructures.

A century ago, Taylor advanced the concept that only certain sites are in fact catalytically active [8]. Nowadays, the concept of active sites is re-evaluated with many attempts to link them with the coordination, shape, and size of the catalyst [9, 10]. This will allow us to more precisely understand and utilize such terms as "turnover frequency" and "structure sensitivity" [11] and a novel concept what could be coined "cluster shape sensitivity". Herein the first usage of magic formulae based on GCNs is shown for platinum nanostructures, leading to reasonable agreement with experiments, thus lending validity to the hypothesis that common GCN sites have similar activity.

Generally, the concept of active sites is divided into geometric and electronic effects [9, 11]. Geometric concepts deal with the structure of the catalytic surface, defects, and shape and size of the nanoparticles. Electronic factors include alloys, band structure, strain-effect of bonding, and doping [12]. Several of these factors have formulas for generalized coordination numbers (GCNs) relating geometric and electronic character. The stress effect of the active sites on activity has been studied on stepped Pt surfaces [13].

In the literature on heterogeneous catalysis the concept of turnover frequency is often used, and the activity is calculated per exposed site. Obviously when the size of a nanoparticle is increasing, the activity per exposed site can change as the relative ratio of active sites with different reactivity (e.g. corners, edges and terraces) is changing. Subsequently the turnover frequency just considering edges, corners and terraces can be expressed as

$$TOF = r_{terrace} \cdot f_{terrace} + r_{edge} \cdot f_{edge} + r_{corner} \cdot f_{corner} \tag{1}$$

where $f_{terrace}$, etc. denote the fractions of these surface sites. In this approach activity is attributed exclusively to changes in the relative contributions of edges, corners and terraces upon size alteration. On a more detailed level not only the size, but also the shape of nanoclusters (e.g. cube, octahedron, cuboctahedron, etc.) for the same overall size defines the reactivity as was demonstrated in the literature for a number of reactions [14, 15, 16, 17, 18]. The fraction of different types of sites for different geometries has been discussed in the literature [3].

If changes in the shapes are taken into account, the overall reaction rate is calculated as the sum of the rates of each active site of type "a" multiplied by its number N_a

$$r = \sum_{a}^{N_s} r_a \cdot N_a \tag{2}$$

where N_s is the total number of types of active sites. Recently such approach was used by Spano and co-workers [19] quantifying the size and shape effects on structure sensitivity in carbon dioxide methanation over nickel-based catalysts. It is apparently clear that while counting the number of sites even for a complex geometric shape might not be problematic, evaluation of catalytic activity is obviously challenging, as reactivity of each and every type of active sites is unknown. From the practical viewpoint there are thus two options to explore cluster shape reactivity. One is related to atomistic structure classification and

site enumeration methodologies, while the second one considers one or few descriptors, like the centrosymmetry parameter [20], bond order parameters [21], or generalized coordination number. The latter one, as already mentioned, is scaled with reaction energies, thus allowing to link the shape of a nanoparticle with its reactivity. The common neighbor analysis (CNA) classifies atoms based on the number of shared nearest neighbors and their bonding. Filot and co-workers [22] used this method to investigate the surface atom arrangements of cobalt nanoparticles focusing on changes of the topological arrangements (namely terrace, step-edge and low-coordinated sites) as a function of the nanoparticles size. It was stated that that the surfaces of smaller particles (e.g. 2 nm) contain atoms that cannot be identified by the CNA algorithm.

In the approach adopted in the current work the generalized coordination numbers GCN were used giving one comparative performance descriptor, on one hand limiting prediction of nanoparticles activity and neglecting the active site distribution, but on the other substantially improving statistical analysis of kinetics constants. Utilization of the GCN can be viewed as some sort of a compromise between a feasible computational approach on one hand and several simplifications, primarily an assumption that the same GCN are catalytically equivalent. It is also important to mention that while in academic literature the main focus is on elucidation of turnover frequency, in industry [23] this descriptor is seldom used and it is mainly mass activity or time-space yield, which is of interest. Worth noting is a special area of catalysis, namely electrocatalysis, where due to high metal loading, mass activity is also of primary concern. Interestingly, in the academic literature [22] the mass activity is applied in addition to turnover frequency. The latter is defined as activity per surface sites and can be recalculated from mass activity, knowing the number of surface sites, which is directly related to the topology, size, and shape of nanoclusters [3].

Platinum is the namesake element of the Platinum Group Metals (PGM) which are known for exceptional catalytic capability [24]. These six elements include three from 4d orbitals, palladium, rhodium, and ruthenium, and from the 5d orbitals, platinum, iridium and osmium. These are rare elements in the Earth's crust, with platinum and palladium having the highest concentration in available ores. Current estimates are that there are about 200 years supply given probable usage, but only 100 years for palladium. Catalysts are key to enabling the Earth's population to grow and simultaneously raising the standard of living over the last century. The vast majority of modern chemicals relevant to daily life use catalysts. Technology has enabled the rise of computational models for theoretical understanding and modeling of chemical reactions, especially using density functional theory (DFT). Experimentally, new techniques such as atomic electron tomography may allow the determination of the 3D coordinates of catalysts' active sites [25].

Experimentally, the size and shape activity of platinum nanoclusters and nanocages has been intensively investigated for the last ten years [26, 27]. The model for the mass activity we present for clusters and cages is the first feasible approach that explains experimental data. Using standard current desktop computers, we model clusters and cages with up to $N \sim 42{,}000$ atoms. This number is constrained by the adjacency matrix in our modeling, which scales as N^2. The ORR may be suitable for study using quantum computing [28], given the limited number of atoms that can be used in a DFT model with classical computers.

Ruthenium catalysis for the NRR

The NRR or synthesis of ammonia from hydrogen and nitrogen;

$$2\,N_2(g) + 3\,H_2(g) \underset{\text{Fe/Ru}}{\overset{500^\circ\text{C, 200 atm}}{\rightleftharpoons}} 2\,NH_3(g)$$

is of such importance to science and agriculture, resulting in production of fertilizers and thus food for a growing population, that it has been awarded two Nobel prizes at the beginning of the 20th century, one for proof of concept (Haber), and another for industrial implementation of the process at high pressure (Bosch). The elusive search for ambient pressure and temperature synthesis [29] may lead to a third. Iron and ruthenium catalysts were found to be most efficient for the synthesis of ammonia by trial and error [30]. Ruthenium is the most efficient, but belongs to the PGMs and their associated scarcity and high cost. Interestingly, ruthenium lies below iron in the Periodic Table. The synthesis of ammonia catalyzed by ruthenium has been studied via first principles (DFT) [30]. Some multiple factors of error between the calculated value and the experimental result were found, part of which may be attributed to the unknown number of active sites on the nanocluster. The size sensitivity of Ru catalysts has been studied [31]. Recently, in-situ operando probing of the surface chemistry confirmed that nitrogen dissociation is the limiting step [32] in line with the Temkin-Pyzhev kinetics of ammonia synthesis suggested almost a century ago. The kinetics of strained Ru nanoparticles has been studied with kinetic Monte Carlo methods in relation to GCNs [7]. A DFT study of trilayer clusters concluded that strained and fcc structures, namely Pd@Re@Ru may lead to an effective ruthenium catalyst [33]. Ruthenium normally has a hcp structure, but can be synthesized with an fcc motif in nanostructures [34, 35]. Such fcc ruthenium clusters and cages appear to have better catalytic properties with respect to the NRR than hcp nanostructures [34]. The hcp structures appear not to have GCN magic formulas, but the fcc ruthenium is expected to be analogous to fcc platinum. We envision a study of nitrogen dissociation by fcc ruthenium for the finite number of GCN sites on nanocages and nanoclusters, using methods similar to Ref [7]. Note that our Euclidean matrix contains 3D coordinates of GCN sites and neighbors. This would then determine the relative kinetics of the different sites and to get the total, one would use the magic formulas for the GCN sites outlined herein this manuscript, yielding size and shape effects not otherwise attainable.

Methods

The current work applies magic formulas to catalysis and structure. The magic formulas related to clusters has previously been studied by Teo and Sloane [36]. They show that counts of surface atoms are of order $\mathcal{O}(n^2)$ where n is the number of shells of the cluster. Magic formulas for clusters has been studied by other authors, cf. [37, 38]. We derive equations in agreement with other results, lending credibility to our techniques. We apply computational methods to derive counts of subsets of surface atoms, i.e. surface generalized coordination numbers.

Ordinary coordination numbers for nanoclusters and nanocages have 'magic' formulas that result from the number of shells and the number of layers in the walls of the nanocage,

which we have recently enumerated [3, 4]. Generalized coordination numbers (GCNs) are an extension of ordinary coordination numbers. Assume there are N_T atoms in the cluster in a fixed order so that each atom is identified by its site index $i \in \{1, \ldots, N_T\}$ and let cn_i be the classical coordination number of site i and $\mathcal{N}_i = \{j_1, \ldots, j_{cn_i}\}$ the corresponding set of nearest neighbors. Then we define the GCN for site i as follows (see [1]):

$$\overline{CN}_i = \sum_{j \in \mathcal{N}_i} \frac{cn_j}{cn_{\max}} \tag{3}$$

where $cn_{\max} = 12$ for top sites. All the nearest neighbors of nearest neighbors of site i are counted and each one contributes $1/cn_{\max}$ to $\overline{CN}_i$. For example, in bulk, where all the sites have coordination $cn_{\max}$ we get $\overline{CN}_i = cn_i = cn_{\max}$. Importantly, it has been shown using DFT that all the adsorption energies of the intermediates involved with ORR are linearly related to GCNs [1, 2]. In developing this research, we have extended the concept of magic formulas for classical coordinations to GCNs of fcc polyhedra and nanocages. The counts of GCNs herein have quadratic polynomials, which we computationally derive. We emphasize that surface GCNs are related to catalytic activity, which this paper describes. Details on our methods are further outlined in the Supplementary Information file.

Results and Discussion

We apply our methods to three distinct cases, namely; A. Polyhedral Clusters, B. Nanocages, and C. Strained Core-Shell Model. These cases define separate structures, resulting in modifications in the application of our techniques.

A. Polyhedral Clusters

Synthesis of platinum nanoclusters with control over the size and shape has been studied for 30 years [39]. Even then it was realized that such control could be advantageous for catalysis. Subsequent years have seen advances in chemical synthesis encompassing all the PGMs and noble metals [26]. An important parameter is the mass activity, which is related to the chemical reactivity per unit mass. The catalytic activity of platinum nanoparticles has been previously studied by DFT as functions of size and shape [40] [41]. These models preceded much of the experimental data that was to follow. We use a model developed by Rück et al., for the mass activity of platinum nanoparticles [5, 6]. A plot of experimental mass activity versus $\overline{CN}$ for relevant platinum surfaces and platinum alloys can be described with a volcano plot having a peak in the data. This volcano plot can then be fit to exponential functions of activity versus $\overline{CN}$. The active sites are those with $7.5 \leq \overline{CN} \leq 8.3$, referred to as the 'Goldilocks Zone' by the current authors. This model fits Pt(111) data best, but we note that (100) surfaces also have catalytic activity. The exponential fit [5], (see the Supplementary Information file) is described by Eq. 4 below,

$$A_{volc}(\overline{CN}_i) = \begin{cases} \exp(3.14\,\overline{CN}_i - 23.40), & 7.5 \leq \overline{CN}_i \leq 8.1, \\ \exp(-4.96\,\overline{CN}_i + 42.18), & 8.1 < \overline{CN}_i \leq 8.3, \\ 0, & \text{otherwise.} \end{cases} \tag{4}$$

The mass activity of a Pt(111) nanostructure is then (m, mass):

$$j_m^{\mathrm{Pt(111)}}(n) \approx \frac{4.116\mathrm{A/mg_{Pt}}}{N_T(n)} \cdot \sum_{7.5 \le \overline{CN}_i \le 8.3} N(\overline{CN}_i, n) \cdot A_{volc}(\overline{CN}_i). \tag{5}$$

Here $N(\overline{CN}_i, n)$ is the polynomial in n related to the GCN $\overline{CN}_i$.

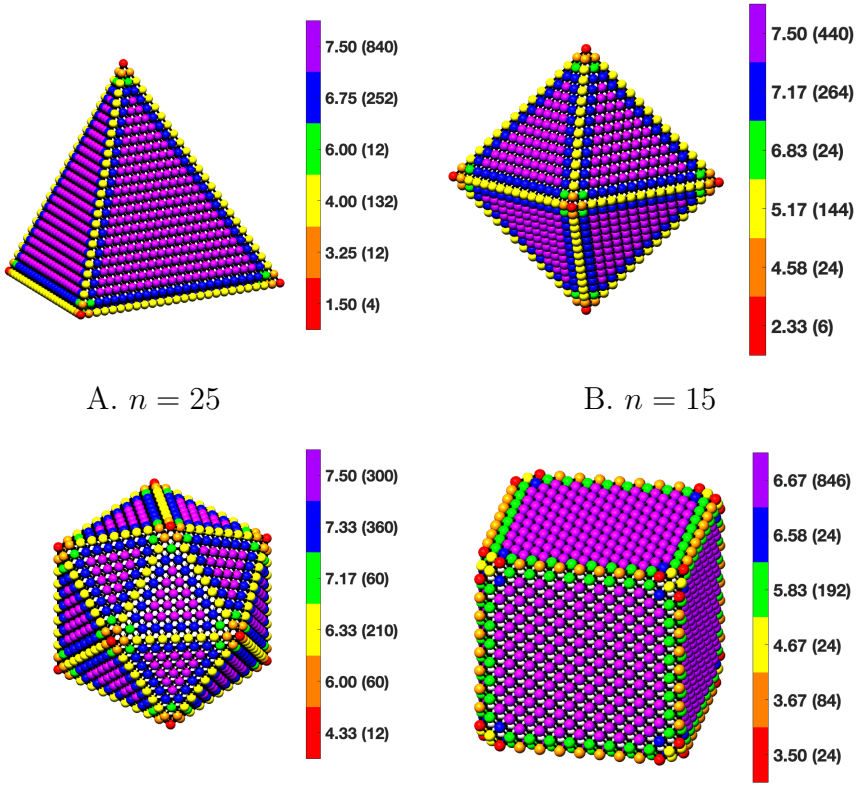

A. $n = 25$ B. $n = 15$

C. $n = 10$ D. $n = 10$

Figure 1: GCN models of polyhedra. A: Tetrahedron, B: Octahedron, C: Icosahedron, D: Truncated Cube. The colorbar gives the GCN surface values and in parenthesis, the count of each value for n, the number of shells.

A similar equation applies to Pt(100) nanocubes, see the SI file:

$$j_m^{\mathrm{Pt(100)}}(n) \approx \frac{2.377\ \mathrm{A/mg_{Pt}}}{N_T(n)} \cdot N(\tfrac{20}{3}, n) \cdot 0.286 \tag{6}$$

where the GCN value $(20/3) \sim 6.67$ is for the (100) facet sites and $N(\frac{20}{3}, n)$ is the quadratic polynomial in n, giving the count of sites whose GCN equals 20/3, while $N_T(n)$ is the cubic polynomial giving the total number of atom sites in the cluster and the activity $A(\frac{20}{3}) = 0.286$.

Figure 1 shows four polyhedra with surface GCN values. The numbers in parentheses represent the count of those GCN values and are associated with magic formulas depending on n. These numbers are counts from which the magic formulas are derived. Of the three structures with (111) symmetry, tetrahedra have the highest proportion of facet atoms (active sites) per unit surface area.

Figure 2 plots mass activity for platinum polyhedra. Tetrahedra have the highest values, and all nanostructures show maxima below $D \sim 10$ nm. We find the magic formulas for GCN = 15/2 and N_T below. The value of GCN = 7.5 is the only number in the Goldilocks Zone for (111) symmetry. The reader is encouraged to verify that the quadratic equations in the numerator of Eqns. 7-10 return the counts in the GCN = 7.5 of Fig. 1. The equations for the mass activity $j_m(n)$ for the four polyhedra are below.

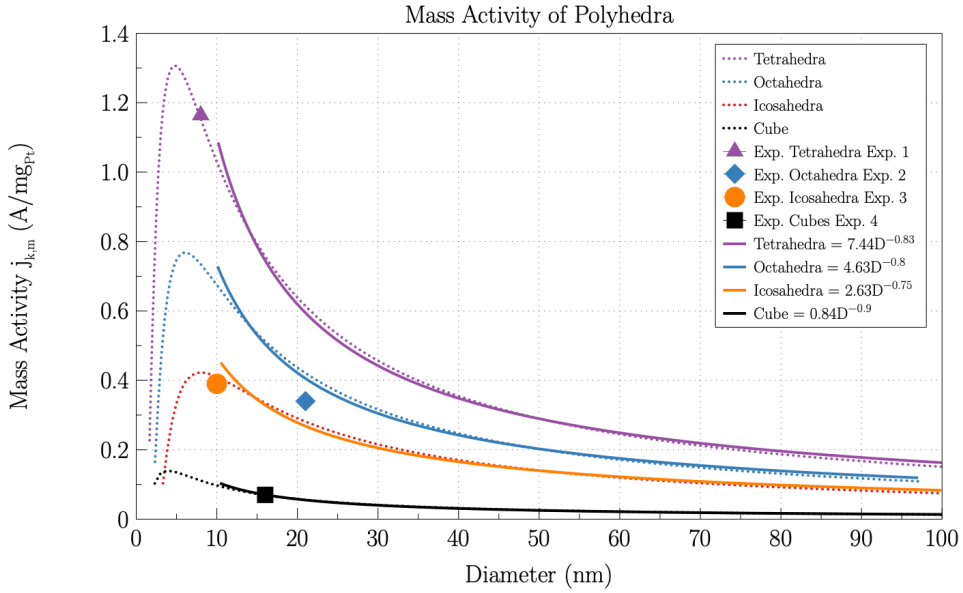

Figure 2: Mass activity of polyhedra. References for experimental data: Exp. 1 [42], Exp. 2 [43], Exp. 3 [44], Exp. 4 [45]. Some of these are core-shell catalysts.

The experimental data in each case is measured from binary core - shell clusters, with a few layers of platinum on palladium nanoclusters. The cube is a data point used for modeling, thus it is an exact fit, see the SI file for details. Table 1 includes data for solid clusters and also cages. The solid curve fit is for power law approximations to the mass activity.

Tetrahedron

$$j_m^T(n) = 4.116 \cdot 1.1618 \cdot \frac{2n^2 - 18n + 40}{\frac{1}{6}n^3 + n^2 + \frac{11}{6}n + 1}, \quad n > 7, \tag{7}$$

Octahedron

$$j_m^O(n) = 4.116 \cdot 1.1618 \cdot \frac{4n^2 - 36n + 80}{\frac{2}{3}n^3 + 2n^2 + \frac{7}{3}n + 1}, \quad n > 7, \tag{8}$$

Icosahedron

$$j_m^I(n) = 4.116 \cdot 1.1618 \cdot \frac{10n^2 - 90n + 200}{\frac{10}{3}n^3 + 5n^2 + \frac{11}{3}n + 1}, \quad n > 7, \tag{9}$$

Cube

$$j_m^C(n) = 2.377 \cdot 0.286 \cdot \frac{12n^2 - 36n + 6}{4n^3 + 6n^2 + 3n - 7}, \quad n > 5, \tag{10}$$

where the activity of Pt(111) and Pt(100) facet sites is given by the values 1.1618 and 0.286, respectively.

For tetrahedra the maximum occurs for $n \sim 17$ or 18, for octahedra a max at $n \sim 16$, for icosahedra $n \sim 15$ and for the cube $n \sim 7$. This is in the range of $D = 5$ – 10 nm, which is in the range for ORR and for other Pt reactions. We also determine that $D = a_s \cdot n_B \cdot n - b_s$ where $a_s = 1$ for tetrahedra, $a_s = 1.414$ for octahedra, and $a_s = 2$ for icosahedra and $n_B = 0.2775$ nm and b_s is dependent on the nanostructure. The term n_B is the bond length for platinum, or for another relevant element. The power law fit in Fig. 2 is reasonable, given that D is linear with n. Related to platinum polyhedra, the synthesis of palladium tetrahedra and octahedra has been studied and can be used for core shell structures with platinum in the outer shell [46].

B. Nanocages

Platinum nanocages, occasionally referred to as nanoboxes, have been studied for the last 10 years [47]. Nanocages are defined by a hollow polyhedral structure with a known number of wall layers. We show here that mass activity is sensitive to the number of wall layers, so that an unambiguous determination of the number of layers is important. Catalytic activity of three nanocage types has been studied, namely icosahedral, octahedral, and cubic cages.

Table 1 presents experimental data for platinum nanoclusters and nanocages. We suggest that the mass activity may be modeled with magic formulas leading to the shape and size dependence as in Figures 2-5. Note that the magic formulas in part B of Figs. 3-5 generate the counts in parentheses in the colorbar of part A. The shape and size model of mass activity is determined by the generalized coordination numbers for the different clusters and cages and the magic formulas that we determine for these $\overline{CN}$. For the cubic cages, we find the activity depends on both the (100) and (111) $\overline{CN}$s. This leads to a rise in activity for smaller D as shown in Fig. 5C. However, this model indicates that for clusters, tetrahedral shapes are favored over other shapes for higher mass activity. For cages, we note that there are $\overline{CN}$s which do not exist for the polyhedra. Thus, octahedral shapes lead to favorable activities over icosahedra or cubes, since there are more active sites in the cluster surface. In contrast to the nanopolyhedra, the magic formulas for the GCNs and N_T related to mass activity of nanocages are quadratic ratios in n, the number of shells and thus the mass activity is constant with increasing D.

Nanocage Ref.	Mass Activity	Specific Activity	D(nm)	Morphology
[47]	0.75	1.98	28	octahedron
[47]	0.37	0.81	35	cubic
[48]	1.28	3.50	18	icosahedron
Nanocluster Ref.	Mass Activity	Specific Activity	D(nm)	Morphology
[42]	1.164	4.770	7	tetrahedron
[49]	0.36	1.10	7.3	octahedron
[43]	0.40	0.67	21	octahedron
[44]	0.39	0.83	10	icosahedron
[45]	0.07	0.35	16	cubic

Table 1: Data for platinum clusters and cages. Mass Activity has units ($\mathrm{A/mg_{Pt}}$) and Specific Activity has units ($\mathrm{mA/cm^2}$).

Our modeling shows that mass activity varies as the number t of wall layers in an inverse relation for large values of n, the number of shells. This is in agreement with our previous work, see [4]. The octahedra have the value $9.3524/t$ and the icosahedra vary like $9.3523/t$ as determined from Figs. 3C and 4C for $D \sim 100$ nm. From [4] we see that the octahedra, icosahedra and cubic nanocages all vary as $2/t$ in the limit for large values of n, with regard to the ordinary coordination. For the cubic nanocages, we get the value $1.5517/t$ for large n or D as determined from Fig. 5C.

Although the mass activity of cages increases with a decreasing number of wall layers, structural integrity is compromised, as mentioned by experimentalists [47]. It was mentioned that aggressive processing caused cages with fewer walls to become fragmented. Thermal stability of cages is good up to $T = 400°$C, as determined by electron microscopy [50], with octahedral cages being more robust than the other shapes.

Figs. 3-5, have experimental data plotted together with the simulated data. For octahedral cages, Fig. 3C, shows a data point from Ref. [47]. Transmission Electron Microscopy (TEM) shows wall layers $t = 7$, with data points labeled Exp. 1 and Exp. 2 in Fig. 3C. The difference in the two values, is that Exp. 2 is adjusted for approximately 20% holes in walls due to processing. TEM showed 7 layers in one of the nanocages, but the distribution of wall layers is not known.

TEM also shows that the octahedra are somewhat truncated as well. The data point, TO (truncated octahedron), is calculated from a truncated octahedron with $t = 7$, see the SI file. This structure does not have magic formulas, so we use counts of GCNs to determine the mass activity. Computationally, we are limited to $D \sim 12$ nm, somewhat smaller than the experimental data. The TO model has mass activity, $j_m^{TO} \sim 1.3$ $\mathrm{A/mg_{Pt}}$.

The experimental data point in Fig. 4C is for icosahedral cages from Ref. [48]. These cages had $t = 7$ with $j_m^I \sim 1.28$ $\mathrm{A/mg_{Pt}}$. This data point has somewhat better agreement with our model than the octahedral data point.

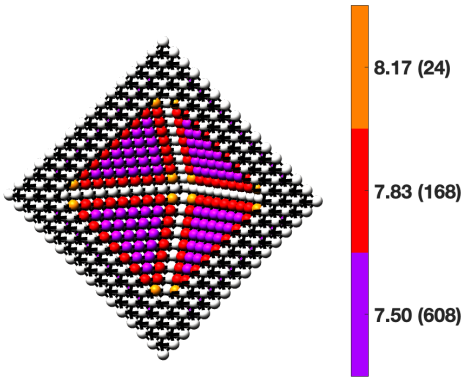

A. Octahedron $n = 15, t = 3$

Octahedron $t = 3$	
Atoms N_T	$12n^2 - 48n + 86,\ n \geq 8$
$\overline{CN} = \frac{15}{2} = 7.5$	$8n^2 - 104n + 368,\ n \geq 8$
$\overline{CN} = \frac{47}{6} = 7.83$	$24n - 192,\ n \geq 8$
$\overline{CN} = \frac{49}{6} = 8.17$	$24,\ n \geq 8$

B. Magic formulas for the $\overline{CN}$

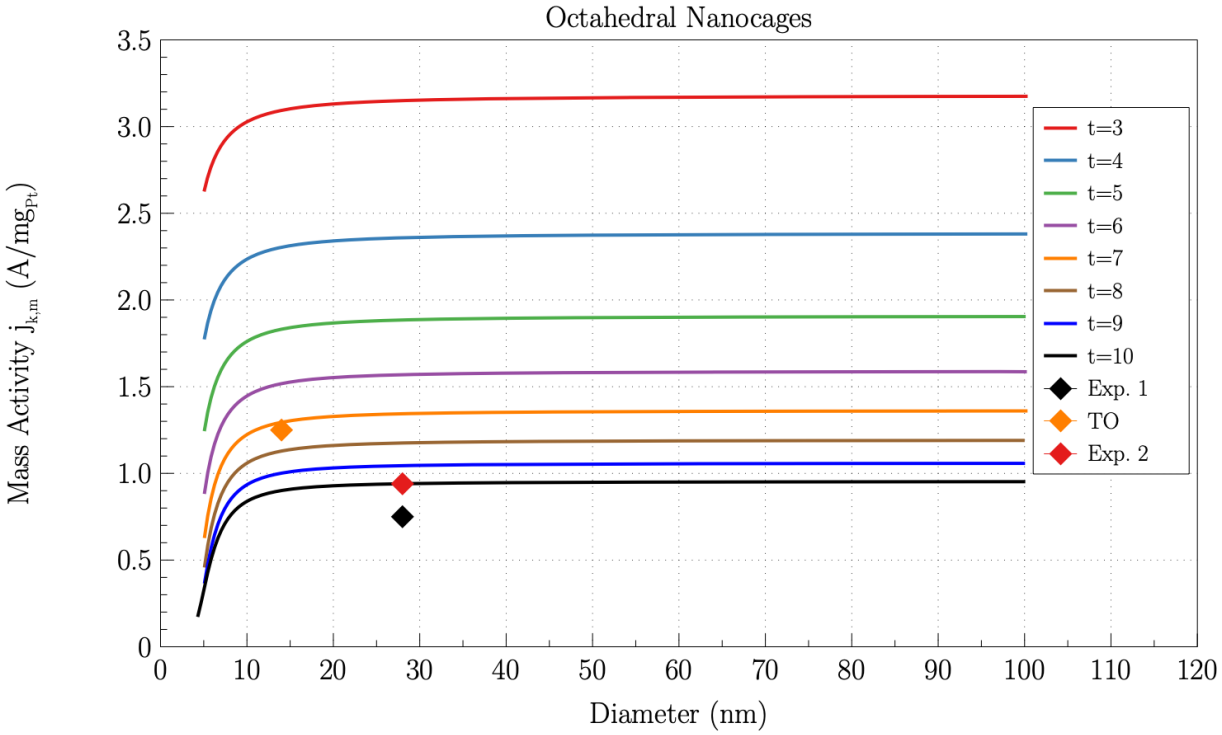

C. Mass Activity for Octahedra with 3 - 10 wall layers.
TO refers to the truncated octahedron, see the SI file. Exp 1 and Exp. 2 from [47].

Figure 3: Simulation results for the Octahedra.

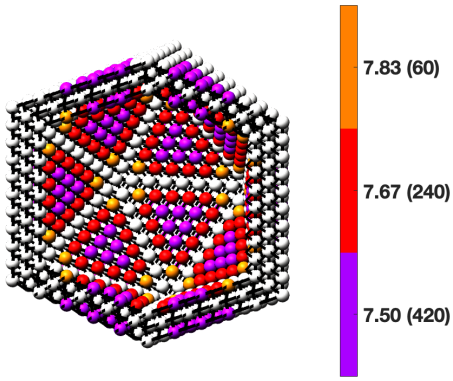

A. Icosahedron $n = 10, t = 3$

Icosahedron $t = 3$	
Atoms N_T	$30n^2 - 60n + 56,\ n \geq 6$
$\overline{CN} = \frac{15}{2} = 7.5$	$20n^2 - 220n + 620,\ n \geq 6$
$\overline{CN} = \frac{23}{3} = 7.67$	$60n - 360,\ n \geq 6$
$\overline{CN} = \frac{47}{6} = 7.83$	$60,\ n \geq 6$

B. Magic formulas for the $\overline{CN}$

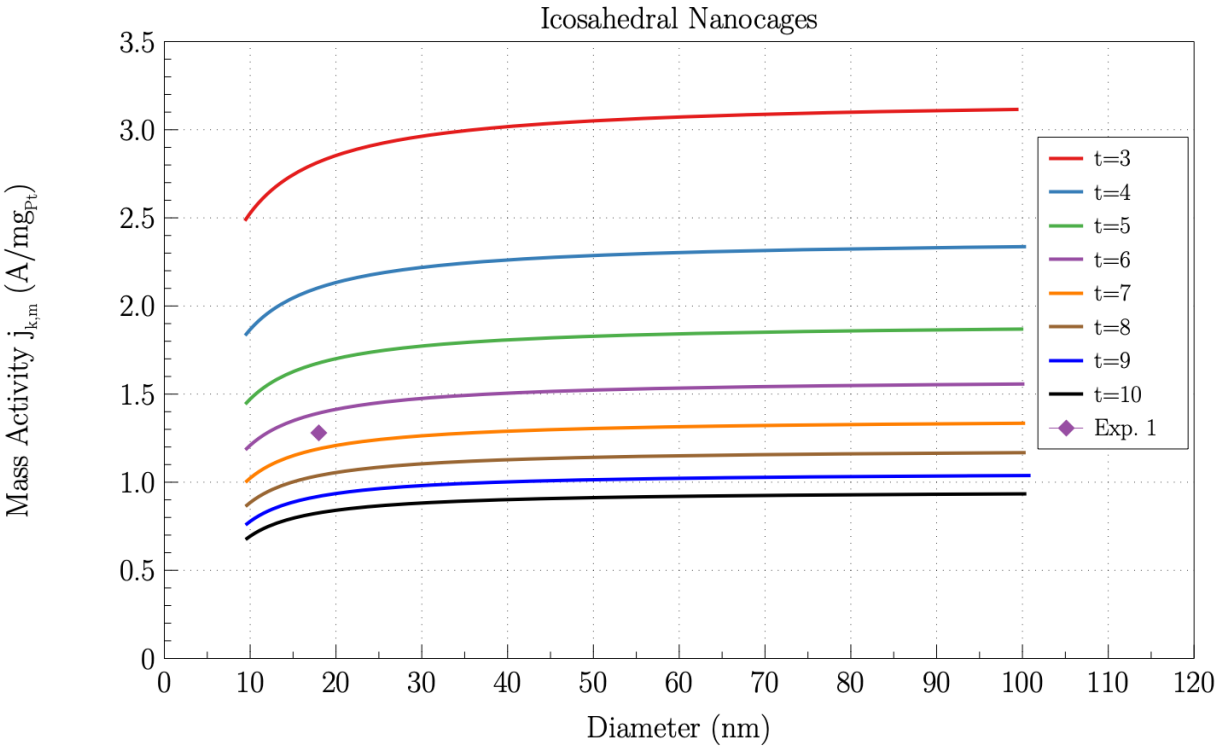

C. Mass activity for Icosahedra with 3 - 10 wall layers. Exp. 1 from [48].

Figure 4: Simulation results for the Icosahedra.

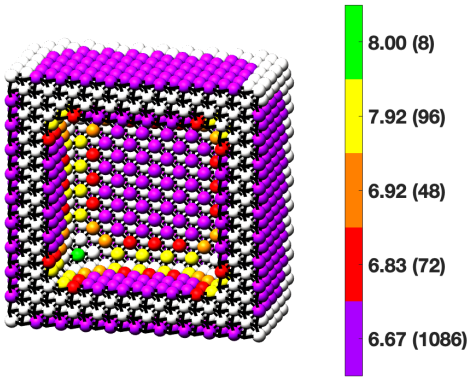

A. Truncated Cube $n = 10, t = 4$

Truncated Cube $t = 4$	
Atoms N_T	$48n^2 - 144n + 172,\ n \geq 6$
$\overline{CN} = \frac{20}{3} = 6.67$	$24n^2 - 168n + 366,\ n \geq 6$
$\overline{CN} = \frac{95}{12} = 7.92$	$24n - 144,\ \ n \geq 6$
$\overline{CN}$=8	$8,\ n \geq 6$

B. Magic formulas for the $\overline{CN}$

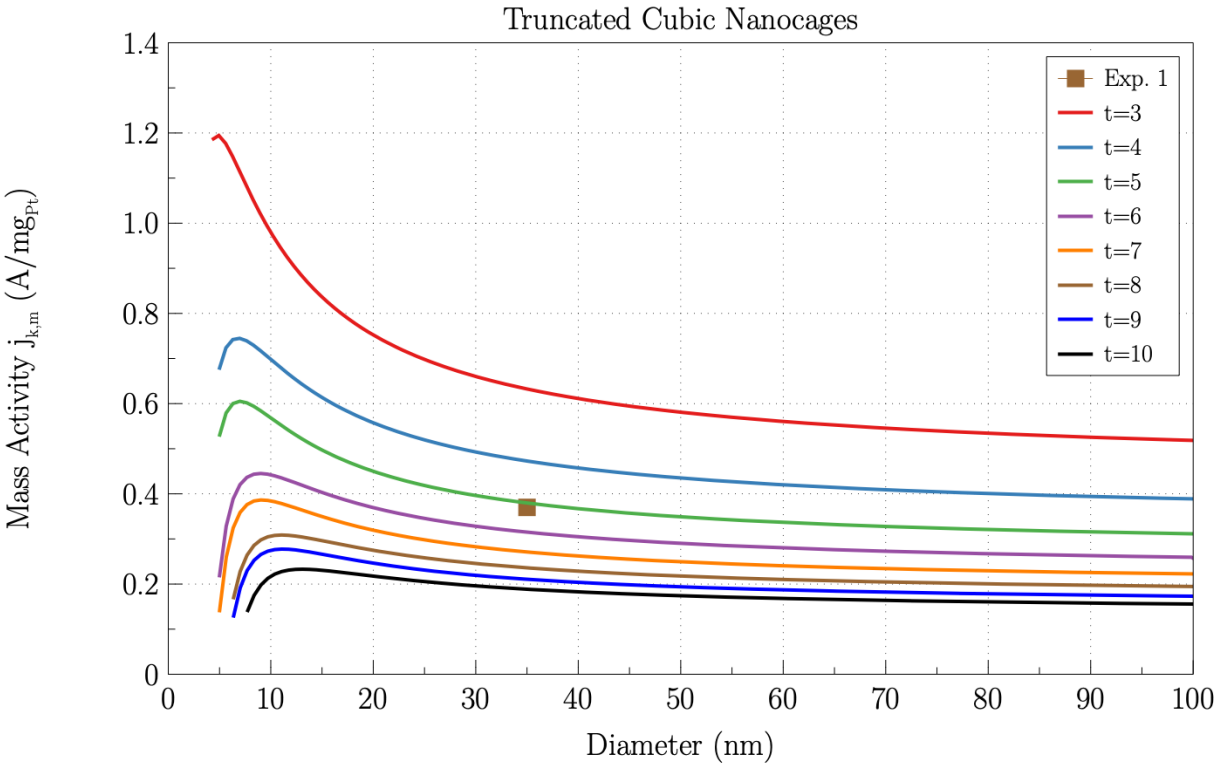

C. Mass activity for the Truncated Cube with 3 - 10 wall layers. Exp. 1 from [47]

Figure 5: Simulation results for the Truncated Cube.

Fig. 5C shows a data point from Ref.[47] for a cubic nanocage for cages with $t = 4$, or 5, or 6. We find the functional form derived from the cube is able to predict the mass activity ($j_m = 0.38\text{A/mg}_{\text{Pt}}$) for $t = 5$ for cubic cages, with $D = 35$ nm. The equation is below,

simply a combination of the two previous equations, Eqn. 5 and Eqn. 6.

$$j_m(n,t) \approx \frac{2.377 \text{ A/mg}_{\text{Pt}}}{N_T(n,t)} N(\tfrac{20}{3},n,t)\cdot 0.238 + \frac{4.116 \text{ A/mg}_{\text{Pt}}}{N_T(n,t)}\cdot[N(\tfrac{95}{12},n,t)\cdot 4.299 + 8\cdot 5.585], \quad (11)$$

where $N(\frac{20}{3},n,t)$ and $N(\frac{95}{2},n,t)$ are the magic formulas for the GCNs equal to 6.67 (on the (100) surface) and 7.92 (in the Goldilocks Zone) which depend on n and t, related to the cage.

Although the colorbar in Fig. 5A shows GCNs (GCN = 6.83, 6.92) in addition to the model (GCN = 6.67, 7.92 and 8), we do not have any way of calculating mass activity related to those GCN values (too many unknown quantities for the number of equations).

The GCN values 7.92 (linear with n) and 8 come from the interior of the cage and contribute to the mass activity, causing a rise in MA for $D < 50$ nm. We also find that Eqn. 3 has even, odd t behavior as is known for ordinary cn, see Ref. [4]. In other words, we find that GCN = 8 appears for even t only, and is insignificant in the mass activity calculation. The agreement here for the experimental value and our calculated one reinforces the hypothesis that Pt(100) facet sites have activity, and that the overall mass activity includes other GCN values.

In our opinion there are some extraneous factors involved in comparing the experimental data with the model since the experimental data comes from a size distribution, a wall integrity factor, and a number of wall layers distribution. Prior to our modeling there was not a relevant model for comparison. Our modeling consists of single clusters and cages, while the experimental data depends on probably unknown distributions. We comment here that the outer walls of a nanocage has coordination less than 12, and thus has less contrast in an electron microscope image, hindering the count of layers. It remains a difficult problem to say with any confidence how the experimental data compares with the model.

C. Strained Core-Shell Model

The superposition of crystal structures has a long history of modeling the strain mismatch between different lattices [51] [52]. In heteroepitaxy this is referred to as misfit strain ($\epsilon = \frac{d_A - d_B}{d_B}$ where d_X is the bond length in bulk between two atoms of type X) and leads to dislocations and defects in the crystal structures. Strain has been linked to the cluster mass activity of the PGMs and noble metals, which are located in the d-orbitals rows of the Periodic Table, giving rise to the d-band model of band theory and its affect on catalysis [53] [54] [55] [56]. In fcc metals, the bond length is proportional to the lattice constant and some relevant data is listed in Table 2 below. For the most part PGM metals are rare and valued for their catalytic properties, thus expensive.

We model trilayer heteroepitaxial clusters with a void and a 'core' of Pd or Ir, an interlayer metal, chosen from Table 2, and an outer shell always Pt. This allows us to calculate a larger D dependence (an increase of 10 nm) of the mass activity by not storing the void atoms in our model. The trilayers are built layer-by-layer so that we may model the changes one layer at a time. We add the void atoms plus the N atoms in the trilayers to get N_T which is used in the calculation of the mass activity.

fcc Metal	Bond Length (nm)	ϵ_{Pd} %	ϵ_{Pt} %
Ag	0.28887	5.50	4.10
Au	0.28837	4.82	3.92
Pt	0.27748	0.86	0.0
Pd	0.27511	0.0	-0.85
Ir	0.27146	-1.32	-2.17
Rh	0.26894	-2.24	-3.08
Cu	0.25561	-7.09	-7.88

Table 2: Data for trilayer fcc metal clusters. The $\epsilon_{Pt} = \frac{d_M - d_{Pt}}{d_{Pt}}$ data is the lattice mismatch.

Vegard's Law gives an estimate for the lattice constant of mixtures that varies linearly with composition [57]. We presume that for heteroepitaxial clusters the bond length may be averaged using weighting factors based on types of atom counts. Consider a structure that consists of three different metal elements which we call A, B and C. Now consider atom i and suppose it is an element A. Its neighbors can be A, B or C elements. Suppose n_A of its neighbors are A metals, n_B neighbors are B metals and n_C neighbors are C metals. Denote by d_{XX} the unconstrained bond length between 2 atoms of metal X. Then we have an atomic count version of Vegard's Law in terms of the bond length which defines the Vegard's distance $d_{veg}(i)$ for atom i as:

$$d_{veg}(i) = \frac{n_A d_{AA} + n_B d_{AB} + n_C d_{AC}}{n_A + n_B + n_C} \tag{12}$$

where

$$d_{AB} = \frac{1}{1+n_B} d_{AA} + \frac{n_B}{1+n_B} d_{BB} \quad \text{and} \quad d_{AC} = \frac{1}{1+n_C} d_{AA} + \frac{n_C}{1+n_C} d_{CC}. \tag{13}$$

The strained coordination number should be determined for all atoms i in the cluster [57]:

$$cn_i^* = \sum_{j \in \mathcal{N}_i} \frac{d_i}{d_{veg}(j)} \tag{14}$$

where $\mathcal{N}_i$ is the set of the cn_i neighbors of i (cn_i is the ordinary coordination number), $d_i = d_A$ is the unconstrained bond length between atoms of the same type A as atom i, and $d_{veg}(j)$ is the Vegard distance of atom $j \in \mathcal{N}_i$. The Vegard distance varies for each atom in the cluster since the coordination of the atoms depends on the local environment.

The strained generalized coordination number, $\overline{CN}_i^*$ for site i is [57, 58]

$$\overline{CN}_i^* = \frac{1}{cn_{\max}} \sum_{j \in \mathcal{N}_i} cn_j^* \tag{15}$$

where $cn_{\max} = 12$ for fcc metals. The activity of the nanocluster is as in Eqn. 4, replacing $\overline{CN}_i$ by $\overline{CN}_i^*$ but it is only calculated in the platinum shell:

$$A_{volc}(\overline{CN}_i^*) = \begin{cases} \exp(3.14\,\overline{CN}_i^* - 23.40), & 7.5 \leq \overline{CN}_i^* \leq 8.1, \\ \exp(-4.96\,\overline{CN}_i^* + 42.18), & 8.1 < \overline{CN}_i^* \leq 8.3, \\ 0, & \text{otherwise.} \end{cases} \tag{16}$$

The mass activity of the core shell (CS) nanostructure is then:

$$j_m^{CS} \approx \frac{4.116\text{A/mg}_{\text{Pt}}}{N_T} \cdot \sum_{i \in \mathcal{P}} A_{volc}(\overline{CN}_i^*) \tag{17}$$

where $\mathcal{P}$ is the set of platinum atoms in the outer shells.

In Fig. 6 below, we show how a monolayer of copper between palladium and platinum changes the surface GCN values by shifting them higher and increasing the activity in the Goldilocks Zone. Since the strain varies by surface coordination and atom location, the colorbar has 'buckets' with GCN values between the minimum and maximum values. The colorbar shows the center of the bucket and the count of GCN values in the associated range of the bucket. In comparing the surface GCN values with Fig. 1, we see that compressive strain is shifting the GCN values to higher numbers, i.e. values with higher activity, thus increasing the mass activity. We comment here that tensile strain has been studied, i.e. a monolayer of gold between palladium and platinum [59]. The strain effect is to lower the GCN values thus the mass activity, but the observed increase was attributed to a chemical interaction, perhaps related to the d-band [54]. Similarly, another chemical interfacial effect looking at an amorphous interlayer of phosphorous has also been studied via DFT [60].

We find the optimum number of interlayer metal layers and number of platinum outer layers is one for the interlayer and two for the platinum see Fig. 7A. An atom in the (111) layers has six bonds in the plane, three below, and three above, unless it is the outermost layer. We calculate strain in the platinum shell by determining the average bond length and then determining the change from bulk platinum. In Fig. 7B the bond strain from changing the interlayer metal is at most -1.25% since there are six bonds in the (111) platinum layer, thus reducing the bond strain in comparison to the copper interlayer's -8% lattice mismatch. Strain in the Pt(111) layer has been determined to correlate with the d-band [61], and we find this data has a linear relationship given by: d-band (eV)$= -2.49 + 0.0361\cdot$ Strain (%).

It is evident from Fig. 8 that a copper interlayer in the trilayer core shell tetrahedra, leads to the highest mass activity in this model. Copper epitaxy on palladium nanocubes has been observed [62] and for Pd(111) surfaces, it is possible to grow about three epitaxial copper layers [63]. Only one is needed for the structures we model. Also, platinum epitaxy has been shown for Pt/Cu(111) up to six layers [64, 65]. In Fig. 8D, we model bilayer Pd@Pt core shell structures with an Ir core, but with multiple Pd layers below the two Pt layers.

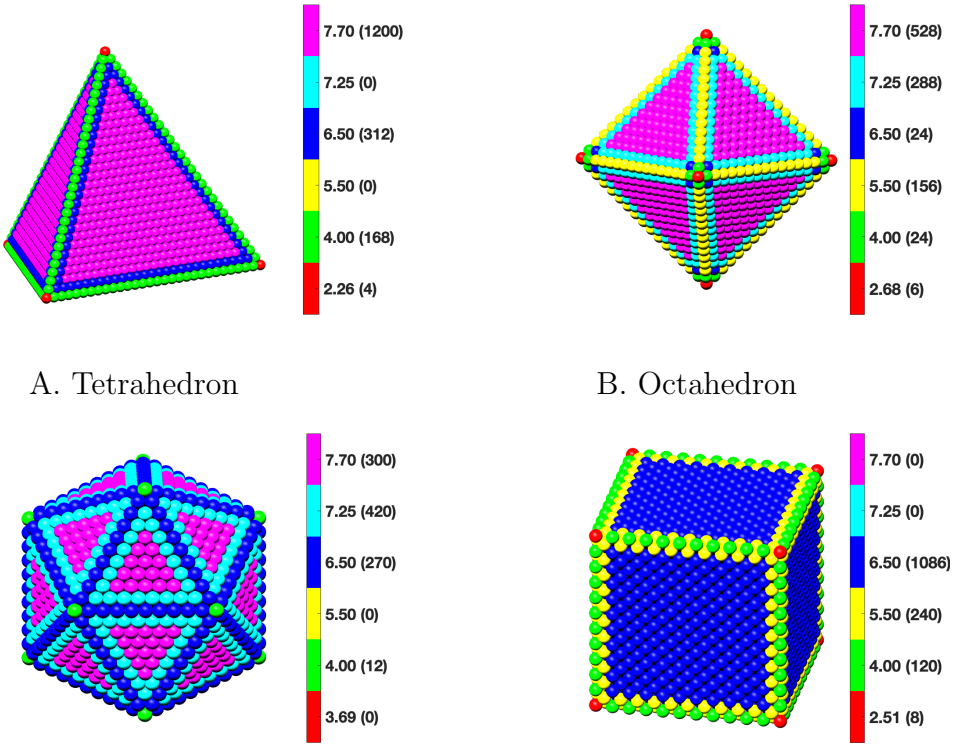

A. Tetrahedron B. Octahedron

C. Icosahedron D. Cube

Figure 6: GCN* models of strained polyhedra (Pd@Cu@Pt).

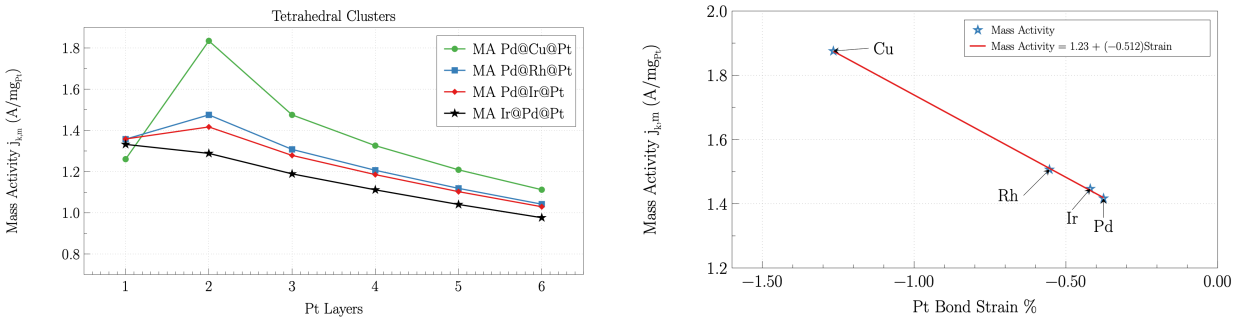

A. B.

Figure 7: A. Mass Activity vs Pt Layers. B. Pt Bond Strain and Mass Activity

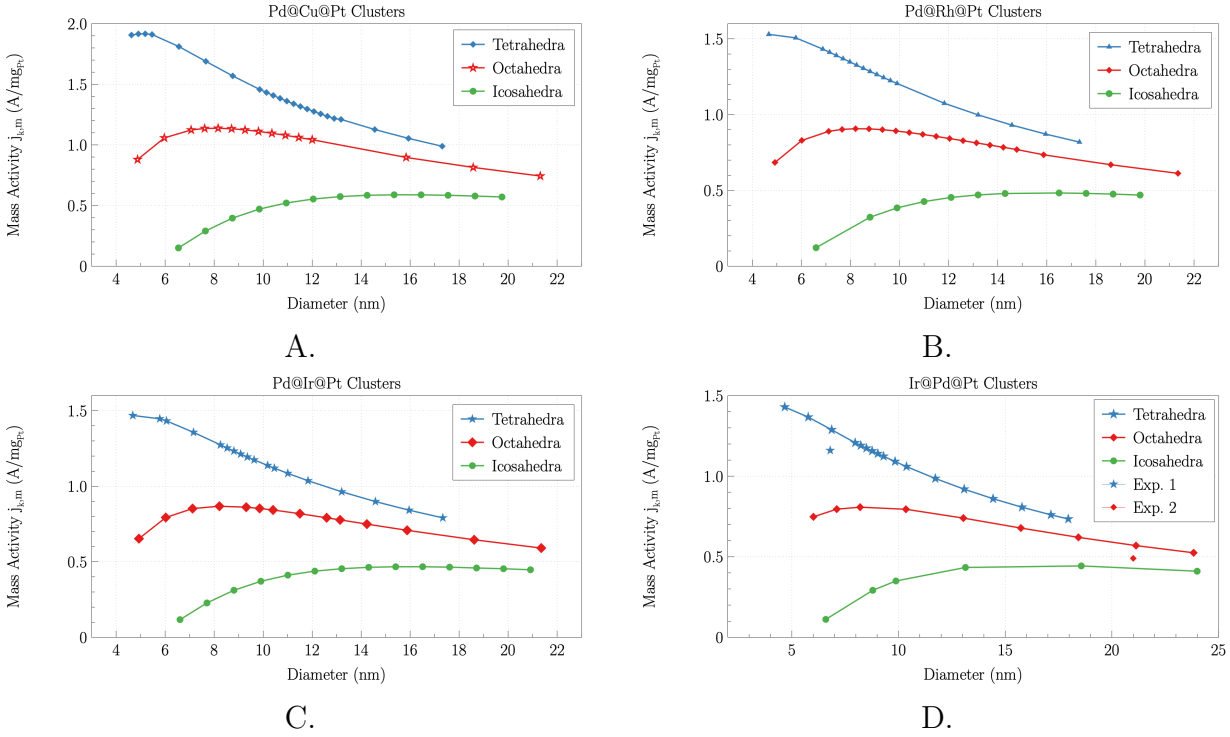

Figure 8: Mass activity as a function of the diameter for 4 cluster structures with the following combination of metals: A: Pd@Cu@Pt, B: Pd@Rh@Pt, C: Pd@Ir@Pt, D: Ir@Pd@Pt. Exp. 1 in D from [42], Exp. 2 from [43].

Tetrahedra of size $D \sim 7$ nm have been synthesized with a measured mass activity of ~ 1.16 A/mg$_{\mathrm{Pt}}$ for the data point Exp. 1 [42]. Additionally, a mass activity equal to ~ 0.49 A/mg$_{\mathrm{Pt}}$ is measured for Pd@Pt octahedra (Exp. 2) with $D \sim 21$ nm [43]. Our modeling presents data with two layers of platinum, and is slightly higher than the experimental data. However, in both experimental data points the number of Pt layers could be more than two, i.e. three which would reduce the mass activity. We calculate for octahedra with $D \sim 22$ nm and 3 Pt layers a mass activity ~ 0.53 A/mg$_{\mathrm{Pt}}$ and for tetrahedra $D \sim 8$ nm with 3 Pt layers a mass activity ~ 1.18 A/mg$_{\mathrm{Pt}}$.

We note that for all three morphologies modeled here, there may not be differences in the mass activity for $D > 25$ nm, as the data converges. The mass activity for the three shapes decreases in the order; tetrahedra, octahedra, icosahedra. This is explained by Fig. 6 where this ordering is due to the number of active sites on the surfaces, i.e. GCN ≥ 7.5.

Conclusions

The simulations described here model single clusters and cages. These nanostructures typically have a lognormal size distribution in TEM images. For the cages we assume that they all have the same number of wall layers. A recommended method of determining the

mass activity of the distribution is to use the size and shape descriptions outlined herein to convert the size histogram to a mass activity histogram, sum it up and divide by the sample size. This method provides a weighted number for the mass activity representing the observed distribution. A comparison can then be made to an experimental measurement. We reiterate that the experimental data comes from a distribution of sizes, wall layers, and sometimes ad hoc estimations of these parameters. Our methods apply to single clusters, and we suggest a more reliable method of determining the activity.

To summarize, we have presented a method of counting the number of GCN active sites for several nanostructures using magic formulas. This leads to a facile procedure of calculating the mass activity for platinum structures. These methods are based on modeling the activity of experimental data and the relationship to generalized coordination numbers. A similar approach has been outlined for fcc ruthenium and the NRR. The size and shape effects calculated with the magic formulas are measurable with standard modern computers leading to reasonably accurate models of activity. Such simplification of counting may lead to better and more efficient catalysts, thus optimizing chemical reactions.

Computational Modeling

All computational modeling uses original code developed by the authors compatible with MATLAB 2025b. Computational code is available from MATLAB Central, see Forrest (2026). GCN Nano (https://www.mathworks.com/matlabcentral/fileexchange/183293-gcn-nano), MATLAB Central File Exchange. Retrieved February 20, 2026.

Conflict of Interest Statement

All authors, FHK, AB, and DYM declare that there is no conflict of interest, financial or otherwise.

Funding

This research did not receive any specific grant from funding agencies in the public, commercial, or not-for-profit sectors.

Author Contributions

FHK conceived of the project, did the data analysis, and wrote the initial draft. AB wrote the MATLAB code. DYM supervised the project. All authors contributed to the final version and approved the article as submitted.

Supplementary Material

Additional discussion and derivation of data used in this manuscript is provided in a freely available pdf.

References

[1] F. Calle-Vallejo, J.I. Martinez, J.M. Garcia-Lastra, P. Sautet, and D. Loffreda. Fast prediction of adsorption properties for platinum nanocatalysts with generalized coordination numbers. *Anew. Chem. Int. Ed.*, 53:8316–8319, 2014.

[2] F. Calle-Vallejo, J. Tyczko, V. Colic, Q.-H. Vu, M.D. Pohl, K. Morgenstern, D. Loffreda1, Ph. Sautet, W. Schuhmann, and A.S. Bandarenka. Finding optimal surface sites on heterogeneous catalysts by counting nearest neighbors. *Science*, 350(6257):185–189, 2015.

[3] F.H. Kaatz and A. Bultheel. Magic mathematical relationships for nanoclusters. *Nanoscale Res. Letters*, 14(1):150, 2019.

[4] F.H. Kaatz and A. Bultheel. Magical mathematical formulas for nanoboxes. *Nanoscale Res. Letters*, 16:39, 2021.

[5] M.Rück, A. Bandarenka, F. Calle-Vallejo, and A. Gagliardi. Oxygen reduction reaction: Rapid prediction of mass activity of nanostructured platinum electrocatalysts. *J. Phys. Chem. Lett.*, 9:4463–4468, 2018.

[6] M.Rück, A. Bandarenka, F. Calle-Vallejo, and A. Gagliardi. Fast identification of optimal pure platinum nanoparticle shapes and sizes for efficient oxygen electroreduction. *Nanoscale Advances*, 1:2901–2909, 2019.

[7] Y. Yang, A. Hellman, and H. Gronbeck. Inherent strain and kinetic coupling determine the kinetics of ammonia synthesis over Ru nanoparticles. *Nature Communications*, 16:1625, 2025.

[8] H.S. Taylor. A theory of the catalytic surface. *Proc. Royal Soc. London A*, 108(745):105–111, 1925.

[9] B. Garlyyev, J. Fichtner, O. Pique, O. Schneider, A.S. Bandarenka, and F. Calle-Vallejo. Revealing the nature of active sites in electrocatalysis. *Chem. Sci.*, 10:8060–8075, 2019.

[10] F. Calle-Vallejo, J.I. Martinez, J.M. Garcia-Lastra, P. Sautet, and D. Loffreda. Why conclusions from platinum model surfaces do not necessarily lead to enhanced nanoparticle catalysts for the oxygen reduction reaction. *Chem. Sci.*, 8:2283, 2017.

[11] C. Vogt and B.M. Weckhuysen. The concept of active site in heterogeneous catalysis. *Nature Reviews Chemistry*, 6:89–11, 2022.

[12] X. Zhu, X. Tan, K-H. Wu, et al. Intrinsic ORR activity enhancement of Pt atomic sites by engineering the d-band center via local coordination tuning. *Angew. Chem. Int. Ed.*, 55(10):18334–18348, 2021.

[13] G. Liu, A.J. Shih, H. Deng, et al. Site-specific reactivity of stepped Pt surfaces driven by stress release. *Nature*, 626:1005–1010, 2024.

[14] S. Cao, F. Tao, Y. Tang, Y. Li, and J. Yu. Size and shape dependent catalytic performances of oxidation and reduction reactions on nanocatalysts. *Chem. Soc. Rev.*, 45:4747–4765, 2016.

[15] C.R. Henry. Morphology of supported nanoparticles. *Prog. Surf. Sci.*, 80:92–116, 2005.

[16] R. Narayanan and M.A. El-Sayed. Shape-dependent catalytic activity of platinum nanoparticles in colloidal solution. *Nano Lett.*, 4:1343–1348, 2004.

[17] A. Sapi, T. Rajkumar, J. Kiss, A. Kukovecs, Z. Konya, and G.A. Somorjai. Metal nanoparticles in heterogeneous catalysis. *Cat. Lett.*, 4:1343–1348, 2021.

[18] B. Roldan Cuenya. Synthesis and catalytic properties of metal nanoparticles: size, shape, support, composition, and oxidation state effects. *Thin Solid Films*, 518:3127–3150, 2010.

[19] G. Spano, M. Ferri, R. Cheula, M. Monai, and B.M. Wechuysen. Deciphering size and shape effects on the structure sensitivity of the CO2 methanation reaction on nickel. *ACS Catalysis*, 15:8194–8203, 2025.

[20] C.L. Kelchner. Dislocation nucleation and defect structure during surface indentation. *Phys. Rev. B*, 58:11085, 1998.

[21] P.J. Steinhardt, D.R. Nelson, and M. Ronchetti. Bond-orientational order in liquids and glasses. *Phys. Rev. B*, 28:784–805, 1983.

[22] M.P.C. van Etten, B. Zijlstra, E.J.M. Henson, and I.A.W. Filot. Enumerating active sites on metal nanoparticles: Understanding the size dependence of cobalt particles for CO dissociations. *ACS Catalysis*, 11(14):8484–8492, 2021.

[23] D. Yu Murzin. Engineering catalysis. *De Gruyter, Berlin*, 3rd Edition, 2026.

[24] A.E. Hughes, N. Haque, S.A. Northey, and S. Giddey. Platinum Group Metals: A review of resources, production and usage with a focus on catalysts. *Resources*, 10:93, 2021.

[25] Y. Yang, J. Zhou, Z. Zhao, et al. Atomic-scale identification of active sites of oxygen reduction nanocatalysts. *Nature Catalysis*, 7:796–806, 2024.

[26] Y. Shi, Z. Lyu, M. Zhao, R. Chen, Q.N. Nguyen, and Y. Xia. Noble-metal nanocrystals with controlled shapes for catalytic and electrocatalytic applications. *Chem Rev.*, 121:649–735, 2021.

[27] M. Zhao, X. Wang, X. Yang, K.D. Gilroy, D. Qin, and Y. Xia. Hollow metal nanocrystals with ultrathin, porous walls and well-controlled surface structures. *Adv. Mater.*, 30:1801956, 2018.

[28] C.D. Paola, E. Plekhanov, M. Krompiec, et al. Platinum-based catalysts for oxygen reduction reaction simulated with a quantum computer. *npj Computational Materials*, 10(285), 2024.

[29] X. Fu, J.B. Pederson, Y. Zhou, et al. Continuous-flow electrosynthesis of ammonia by nitrogen reduction and hydrogen oxidation. *Science*, 379:707–712, 2023.

[30] K. Honkala, A. Hellman, I.N. Remedikis, et al. Ammonia synthesis from first-principles calculations. *Science*, 307:555–558, 2005.

[31] L. Li, Y.F. Jiang, T. Zhang, et al. Size sensitivity of supported Ru catalysts for ammonia synthesis: From nanoparticles to subnanometric clusters and atomic clusters. *Chem*, 8:749–768, 2022.

[32] C.M. Goodwin, P. Lomker, D. Degerman, et al. Operando probing of the surface chemistry during the Haber–Bosch process. *Nature*, 625:282–290, 2024.

[33] S. Kim, M.C. Kim, B.C. Yeo, and S.S. Han. High-throughput design of bimetallic core-shell catalysts for the electrochemical nitrogen reduction reaction. *J. Mater. Chem. A*, 11:24686, 2023.

[34] M. Zhao, L. Xu, M. Vera, et al. Synthesis of Ru icosahedral nanocages with a face-centered-cubic structure and evaluation of their catalytic properties. *ACS Catal.*, 8:6948–6960, 2018.

[35] M. Zhao and Y. Xia. Crystal-phase and surface-structure engineering of ruthenium nanocrystals. *Nature Reviews Materials*, 5:440–459, 2020.

[36] B.T. Teo and N.J.A. Sloane. Magic numbers in polygonal and polyhedral clusters. *Inorg. Chem.*, 24:4545–4558, 1985.

[37] R. van Hardeveld and F. Hartog. The statistics of surface atoms and surface sites on metal clusters. *Surf. Sci.*, 15:189–230, 1969.

[38] J.M. Montejano-Carrizales, F. Aguilera-Granja, and J.L. Moran-Lopez. Direct enumeration of the geometrical characteristics of clusters. *NanoStruct. Mater.*, 8(3):269–287, 1997.

[39] T.S. Ahmadi, Z.L. Wang, T.C. Green, A. Henglein, and M.A. El-Sayed. Shape-controlled synthesis of colloidal platinum nanoparticles. *Science*, 272:1924–1926, 1996.

[40] G.A. Tritsaris, J. Greeley, J. Rossmeisl, and J.K. Norskov. Atomic-scale modeling of particle size effects for the oxygen reduction reaction on Pt. *Catal. Lett.*, 141:909–913, 2011.

[41] V. Tripkovic, I. Cerri, T. Bligaard, and J. Rossmeisl. The influence of particle shape and size on the activity of platinum nanoparticles for oxygen reduction reaction: A density functional theory study. *Catal. Lett.*, 144:380–388, 2014.

[42] K. Su, H. Zhang, S. Qian, J. Li, J. Zhu, Y. Tang, and X. Qiu. Atomic crystal facet engineering of core-shell nanotetrahedrons restricted under sub-10 nanometer region. *ACS Nano*, 15:5178–5188, 2021.

[43] J. Park, L. Zhang, S-I. Choi, L.T. Roling, N. Lu, J.A. Herron, S. Xie, J. Wang, M.J. Kim, M. Mavrikakis, and Y. Xia. Atomic layer-by-layer deposition of platinum on palladium octahedra for enhanced catalysts toward the oxygen reduction reaction. *ACS Nano*, 9(3):2635–2647, 2015.

[44] C.-T. Lee, H. Wang, M. Zhao, T.-H. Yang, M. Vara, and Y. Xia. One-pot synthesis of $PdPt_{nL}$ core-shell icosahedral nanocrystals in high throughput through a quantitative analysis of the reduction kinetics. *Chem. Eur. J.*, 25:5322–5329, 2019.

[45] S.Xie, S.-I. Choi, N.Lu, et al. Atomic layer-by-layer deposition of Pt on Pd nanocubes for catalysts with enhanced activity and durability toward oxygen reduction. *Nano Lett.*, 14:3570–3576, 2014.

[46] Y. Wang, S. Xie, J. Liu, J. Park, C.Z. Huang, and Y. Xia. Shape-controlled synthesis of palladium nanocrystals: A mechanistic understanding of the evolution from octahedrons to tetrahedrons. *Nano Lett.*, 13:2276–2281, 2013.

[47] L. Zhang, L.T. Roling, X. Wang, M. Vara, M. Chi, J.Liu, S-I. Choi, J. Park, J. A. Herron, Z. Xie, M. Mavrikakis, and Y. Xia. Platinum-based nanocages with subnanometer-thick walls and well-defined, controllable facets. *Science*, 349(6246):412–416, 2016.

[48] X. Wang, L. Figueroa-Cosme, X. Yang, M. Luo, J. Liu, Z. Xie, and Y. Xia. Pt-based icosahedral nanocages: Using a combination of (111) facets, twin defects, and ultrathin walls to greatly enhance their activity toward oxygen reduction. *Nano Lett.*, 16(2):1467–1471, 2016.

[49] E. Hornberger, V. Mastronardi, R. Brescia, P. P. Pompa, M. Klingenhof, F. Dionigi, M. Moglianetti, and P. Strasser. Seed-mediated synthesis and catalytic ORR reactivity of facet-stable, monodisperse platinum nano-octahedra. *ACS Appl. Energy Mater.*, 4:9542–9552, 2021.

[50] M. Vara, X. Wang, J. Howe, M. Chi, and Y. Xia. Understanding the stability of Pt-based nanocages under thermal stress using in situ electron microscopy. *ChemNanoMat*, 4:112–117, 2018.

[51] J. Zhao, B. Chen, and F. Wang. Shedding light on the role of misfit strain in controlling core-shell nanocrystals. *Adv. Mater.*, 32:2004142, 2020.

[52] X. Yang, Y. Wang, X. Tong, and N. Yang. Strain engineering in electrocatalysts: Fundamentals, progress, and perspectives. *Adv. Energy. Mater.*, 12:2102261, 2022.

[53] F.H.B. Lima, J. Zhang, M. H. Shao, K. Sasaki, M. B. Vukmirovic, E. A. Ticianelli, and R. R. Adzic. Catalytic activity-d-Band center correlation for the O_2 reduction reaction on platinum in alkaline solutions. *J. Phys. Chem. C*, 111:404–410, 2007.

[54] M.P. Hyman and J.W. Medlin. Effects of electronic structure modifications on the adsorption of oxygen reduction reaction intermediates on model Pt(111)-alloy surfaces. *J. Phys. Chem. C*, 111:17052–17060, 2007.

[55] E. Toyoda, R. Jinnouchi, T. Hatanaka, Y. Morimoto, K. Mitsuhara, A. Visikovskiy, and Y. Kido. The d-Band structure of Pt nanoclusters correlated with the catalytic activity for an oxygen reduction reaction. *J. Phys. Chem. C*, 115:21236–21240, 2011.

[56] S. Jiao, X. Fu, and H. Huang. Descriptors for the evaluation of electrocatalytic reactions: d-Band theory and beyond. *Adv. Funct. Mater.*, 2107651, 2021.

[57] M.Rück, B. Garlyyev, F. Mayr, A.S. Bandarenka, and A. Gagliardi. Oxygen reduction activities of strained platinum core-shell electrocatalysts predicted by machine learning. *J. Phys. Chem. Lett.*, 11:1773–1780, 2020.

[58] F. Calle-Vallejo and A.S. Bandarenka. Enabling generalized coordination numbers to describe strain effects. *ChemSusChem*, 11:1824–1828, 2018.

[59] M. Shao, A. Peles, and J. Odell. Enhanced oxygen reduction activity of platinum monolayer with a gold interlayer on palladium. *J. Phys. Chem. C*, 118:18505–18509, 2014.

[60] S. Ji, C. Zhang, R. Guo, et al. Effect of interfacial interaction on electrocatalytic activity and durability of Pt-based core-shell nanocatalysts. *ACS Catal.*, 14:11721–11732, 2024.

[61] H. Wang, S. Hu, C. Tsai, et al. Direct and continuous strain control of catalysts with tunable battery electrode materials. *Science*, 354:1031–1036, 2016.

[62] M. Jin, H. Zhang, J. Wang, X. Zhong, N. Lu, Z. Li, Z. Xie, M.J. Kim, and Y. Xia. Copper can still be epitaxially deposited on palladium nanocrystals to generate core shell nanocubes despite their large lattice mismatch. *ACS Nano*, 6(3):2566–2573, 2012.

[63] A. de Siervo, R. Paniago, E.A. Soares, H.-D. Pfannes, R. Landers, and G.G. Kleimann. Growth study of Cu/Pd(111) by RHEED and XPS. *Surface Science*, 575:217–222, 2005.

[64] Y.G. Shen, D.J. O'Connor, K. Wandelt, and R.J. MacDonald. Thin film growth of Pt on Cu(111): a LEIS study. *Surface Science*, 357-358:921–925, 1996.

[65] A. Miszczuk, I. Morawski, M. Jurczyszyn, and M. Nowicki. Properties of Pt on Cu(111) revealed by AES, LEED, and DEPES. *Journal of Electron Spectroscopy and Related Phenomena*, 223:29–36, 2018.